One-Minute Whole-Brain Magnetization Transfer Ratio Imaging with Intrinsic B_1-Correction

Roya Afshari*[1,2], Francesco Santini[1,2], Rahel Heule[3], Craig H. Meyer[4], Josef Pfeuffer[5], Oliver Bieri[1,2]

[1]Division of Radiological Physics, Department of Radiology, University Hospital Basel, University of Basel, Basel, Switzerland.
[2]Department of Biomedical Engineering, University of Basel, Basel, Switzerland.
[3]High Field Magnetic Resonance, Max Planck Institute for Biological Cybernetics, Tübingen, Germany
[4]Department of Biomedical Engineering, University of Virginia, Charlottesville, Virginia, USA
[5]Siemens Healthcare, Application Development, Erlangen, Germany.

Submitted to **Magnetic Resonance in Medicine** for possible publication as **Full paper**.

Paper details: Abstract 250 words (max 250), Paper Body 2911 Words (max 5000), 8 Figures (max 10), 41 References.

Keywords: magnetization transfer, MTR, histogram, spiral, B1 mapping, correction, brain.

***Corresponding author:**
Roya Afshari
Division of Radiological Physics, Department of Radiology, University Hospital Basel
Petersgraben 4, 4031 Basel, Switzerland
E-mail: roya.afshari@unibas.ch

Running title: One-Minute Whole-Brain MTR with Intrinsic B_1-Correction.

Abstract

Purpose: Magnetization transfer ratio (MTR) histograms are widely used for the assessment of diffuse pathological changes in the brain. For broad clinical application, MTR scans should not only be fast but confounding factors should be minimized for high reproducibility. To this end, a one-minute whole brain spiral MTR method with intrinsic B_1-field correction is introduced.

Methods: A spiral multi-slice spoiled gradient echo sequence with adaptable magnetization transfer (MT) saturation pulses (angle β) is proposed. After a low-resolution single-shot spiral readout and a dummy preparation period, high-resolution images are acquired using an interleaved spiral readout. For whole brain MTR imaging, fifty interleaved slices with three different MT contrasts ($\beta = 0°, 350°, 550°$) together with an intrinsic B_1-field map are recorded in 58.5s on a clinical 3T system. From the three contrasts, two sets of MTR images are derived and used for subsequent B_1 correction, assuming a linear dependency on β. For validation, a binary spin bath model is used.

Results: For the proposed B_1-correction scheme, numerical simulations indicate for brain tissue a decrease of about a factor of ten for the B_1-related bias on MTR. As a result, upon B_1-correction, MTR differences in gray and white matter become markedly accentuated and the reproducibility of MTR histograms from scan-rescan experiments is improved. Furthermore, B_1-corrected MTR histograms show a lower variability for age-matched normal appearing brain tissue.

Conclusion: From its speed and offering intrinsic B_1-correction, the proposed method shows excellent prospects for clinical studies that explore MT-effects based on MTR histogram analysis.

Introduction

Magnetization transfer (MT), reflecting the exchange of magnetization between mobile and bound protons (1), has shown potential for the diagnosis and prognosis of various neurological disorders, such as multiple sclerosis (for a comprehensive overview, c.f. (2)). Frequently, due to time constraints in the clinical workflow, MT effects are condensed into a simple measure in percent unit (pu), termed magnetization transfer ratio (MTR), that can be derived using only two scans performed with and without saturation of the bound pool protons, respectively (3).

MTR imaging has been extensively explored to track morphological changes in brain, such as for the development of myelination in children (4) or within the context of aging (5), for the detection of microstructural damage in normal appearing white matter (3,6–9), or for the detection of a variety of brain disorders, such as Alzheimer's disease (10) and predominantly multiple sclerosis (MS) (3,11–14). In this context, MTR histograms have proven to be highly indicative of both focal (15) and diffuse tissue damage (13,15–18). Moreover, they allow a distinction of different stages of MS disease (16), a differentiation of MS subgroups (17,18), an estimation of disease burden (19), or a correlation with microscopic changes in gray matter (GM) and white matter (WM) due to aging (20).

It appears evident that a prerequisite for reliable detection of subtle changes in the MTR histogram is a minimization of any confounding factor, such as transmit field (B_1) inhomogeneity or settings of the MT pulse (21). Due to safety limits for power deposition on patients, pulsed rather than continuous wave irradiation is used for MT contrast generation (22,23). This results in a strong but generally incomplete saturation of the bound proton pool. As a result, the observable amount of saturation transfer does thus depend on the off-resonance and the delivered irradiation power, which is locally modulated by B_1 (24,25).

Thus, several approaches were proposed to address B_1-field related variations in MTR values. As a general recommendation, the body coil should be used for transmission (21). Particularly, at high fields, however, object-related B_1-field inhomogeneity becomes more pronounced and appropriate correction of excitation field nonuniformity appears mandatory for accurate estimation of MT effects. To this end, different approaches were suggested to account and correct for B_1-field related MT miscalibrations (24,26–28). Especially, for proton-density weighted spoiled gradient echo (SPGR) MTR acquisitions, a linear correction was found to be adequate (24,27).

For broad clinical translation, MTR scanning should be performed in a reasonable time, ideally without the need for the acquisition of a separate, additional, B_1-field map. In contrast to Cartesian imaging, spiral trajectories might offer a considerable increase in the overall acquisition speed and have found application for rapid tissue quantification, such as MR fingerprinting (29), or for whole brain B_1-field corrected T_1 mapping within less than one minute (30). In this work, we explore the prospects of a one-minute spiral imaging protocol for whole brain MTR imaging with intrinsic B_1-correction.

Methods

Spiral MT sequence

For rapid whole-brain MTR imaging, a prototype interleaved 2D multi-slice SPGR sequence with dual-density spiral-out trajectory (31,32) at a receive bandwidth of 400 kHz was implemented. The spiral trajectory was calibrated in a one-time process using the Tan-Meyer eddy current model (33).

For B_1-correction of MTR, low resolution B_1 mapping was combined with the acquisition of two MTR scans. The two MTR scans were derived from three repetitions of the same sequence using a non-MT-weighted scan and two scans with different off-resonance saturation (angle: β) (Figure 1A). To mitigate possible slice cross-talk and excitation-related MT-effects in neighboring slices, each repetition features two concatenations enabling an interleaved slice excitation scheme for the prototype sequence. For each slice, a B_1 map was derived from the acquisition of two low-resolution PD-weighted images with nominal flip angles of 90° (PD_1 in Rep1) and 45° (PD_2 in Rep2) using a single-shot spiral readout (Figure 1C). The single-shot contrast image in repetition three is acquired but currently not used for the calculations. A recovery period of about 4 s between repetitions one and two is used to allow for recovery of residual slice cross talk effects in the second single-shot contrast image from the acquisition of the second concatenation in repetition one (Figure 1B and Figure 1C). After the single-shot spiral acquisition, the subsequent interleaved spiral readout preceded a dummy period of about 2 s (MT-preparation, slice excitation and gradients are played out, but no readout is performed) to mitigate transient effects (Figure 1C). The TR was set to 650 ms, offering space for the acquisition of 25 interleaved slices within one concatenation (Figure 1D). For MT preparation, a Gaussian-shaped off-resonance irradiation pulse of 7.68 ms duration was used (off-resonance Δ = 2.2 kHz). Generally, 3-mm slices with an in-plane resolution of 1.3 ×1.3 mm^2 (field-of-view: 256 × 256 mm^2) were acquired using a sinc-shaped RF pulse of 2 ms duration, with a time-bandwidth product of 2.7 and a nominal flip angle α of 35°. Single-shot and interleaved spiral imaging was performed with readout durations of 18.24 ms and 7.88 ms, respectively.

For MTR imaging, 20 spiral interleaves in combination with an acceleration factor R = 2 were used, thus effectively reducing the number of required spiral interleaves by 50%. The acquisition time for one concatenation was 9.1 s (including the single-shot spiral readout, the dummy preparation period, and the spiral interleaves). The overall acquisition time for the complete scan was 58.5 s (for three repetitions and the recovery).

In-vivo imaging

Imaging was performed on three healthy volunteers (a female at age 28 and two males at ages 31 and 32) at 3T (Magnetom Prisma, Siemens Healthcare, Erlangen, Germany) using a 20-channel receive

head coil and approved by the local ethics committee. From a single scan, three repetitions performed with nominal MT-saturation flip angles of 0°, 350° and 550°. In addition, a standard T_1-weighted scan (MPRAGE (34)) was acquired for brain segmentation.

To test the scan-rescan repeatability and reproducibility, the MTR scan was first run 10 times without breaks and then 10 times with short breaks by taking the volunteer out after every single acquisition (repositioning), and thus forcing a new scanner adjustment. Subsequently, scan-rescan data was co-registered and an MTR histogram analysis was performed for segmented whole-brain, WM and GM. Peak positions were extracted from the segmented GM and WM MTR histograms using non-linear least-squares fitting of a simple Gaussian distribution (21). Subsequently, standard deviation and coefficient of variation (cv: standard deviation over mean of the peak positions) were calculated and boxplots were generated for the assessed peak positions, serving as indicators of repeatability for the scan-rescan experiment.

Image reconstruction, postprocessing and simulations

Spiral image reconstruction was performed online using a spiral version of the iterative self-consistent parallel imaging reconstruction method (SPIRiT) (35). An auto-stop criterion was used, also in case the k-space was fully sampled at the Nyquist rate, to implicitly derive the optimal density compensation function for the gridding algorithm.

Image post-processing and simulation were performed using MATLAB R2019a (The MathWorks, Inc., Natick, MA). For skull stripping, WM and GM segmentation of the T_1-weighted (MPRAGE) images, and co-registration of the derived masks to the spiral-MT image, the standard software package FSL (FMRIB Software Library v6.0, Oxford, UK) was used.

From the signal intensities of the two low-resolution single-shot PD-weighted spiral scans acquired in repetition one and two (PD_1 and PD_2), B_1 can be estimated using (36)

$$B_1 = \zeta \cdot (4/\pi) \cdot \cos^{-1}\left(\frac{PD_1}{2 \cdot PD_2}\right) \quad [1]$$

where ζ = 1.15 takes into account the exact excitation profile and was derived using CoMoTk (37) and is approximately constant within the expected typical B_1 range (variation is less than 1% within B_1 = 0.7 – 1.3). Only the first concatenation was used for B_1 calculation.

Two sets with different MTR contrast can be derived from the interleaved spiral images (I) acquired within the three repetitions with variable MT-saturation flip angles of β_0 = 0°, β_1 = 350° and β_2 = 550° (c.f. Figure 1),

$$MTR_{1,2} = \frac{I_0 - I_{1,2}}{I_0}\ , where\ I_{0,1,2} = I(\beta_{0,1,2}) \quad [2]$$

Assuming a linear dependency of the observable MTR contrast for a reasonable range of flip angle modulations of the MT-preparation pulse, a B_1-corrected MTR image (MTR_c) can be derived using

$$MTR_c = MTR_{avg} + (1 - B_1) \cdot b \cdot \Delta MTR \quad [3]$$

where $MTR_{avg} \triangleq (MTR_1 + MTR_2)/2$, $\Delta MTR \triangleq MTR_2 - MTR_1$, and $b \triangleq 0.5 \cdot (\beta_1 + \beta_2)/(\beta_2 - \beta_1)$.

The linear (first order) correction proposed in Eq. [3] also requires that the B_1-related change in the observable MTR contrast is dominated by the variation of the saturation pulse amplitude only, i.e.

$$\partial_{B_1} MTR(B_1\alpha, B_1\beta) \approx \partial_{B_1} MTR(\alpha, B_1\beta) \quad [4]$$

which appears reasonable for PD to mildly T_1-weighted images (27). To this end, numerical simulations of the binary spin-bath model were performed with MATLAB as described in details elsewhere (38) assuming ideal spoiling for the free pool and using [$M_{0,r}$ = 0.137; $T_{2,r}$ = 12 μs, $R_{1,r}$ = 1 s^{-1}, k_f = 4.3 s^{-1}; R_1 = 1.17] for WM and [$M_{0,r}$ = 0.062; $T_{2,r}$ = 10μs, $R_{1,r}$ = 1s^{-1}, k_f = 1.8 s^{-1}; R_1 = 0.803] for GM at 3T. Observable T_1 tissue parameters for bulk GM (1264 ms) and bulk WM (838 ms) at 3T were taken from (30). For tissues, a super-Lorentzian lineshape was used. Simulations took into account the actual slice excitation profile and were performed with the spiral MT pulse sequence parameters (cf, "spiral MT sequence") until a steady state was reached.

Results

The sequence provided artifact-free images in all volunteers. Example results are shown in Figure 2. As compared to the non-MT weighted images (Figure 2A), MT-weighted images show increasing MT contrast for tissues (and thus incomplete saturation) with increasing MT-saturation flip angles (Figures 2B and 2C). Typically, over the whole brain, nominal MT-saturation flip angles were modulated by the B_1 field by as much as ±30% (cf. Figure 2D). Visual comparison of the images showed a change in the MTR contrast similar in magnitude to the modulation of the B_1 field. As the measured B_1 differences were as large as ±30%, they corresponded to an approximate range of effective MT-saturation flip angles from 350° to 550°.

The simulated sensitivity of MTR on B_1 is specific for the TR and flip angle used (see 'In-vivo imaging' in the 'Methods' section) and is shown in Figure 3 for GM and WM. Generally, both GM and WM MTR show a slight non-linear dependency on B_1 and increase with increasing B_1. From the two-pool model simulation, the expected B_1-related variation in MTR (for B_1 = 0.7 to B_1 = 1.3) is about 16 – 17 pu (for GM and WM, respectively) and decreases to about 2 pu upon B_1-correction. Overall, the simple

linear correction scheme, as proposed in Eq. [3], is able to reduce B_1-related MTR variations by almost a factor of ten.

Average MTR images (MTR_{avg}), B_1-corrected MTR images (MTR_c), as well as absolute difference images are shown in Figure 4. For regions with a B_1 close to 1 no difference is observed, whereas uncorrected MTR_{avg} values are overestimated for the deep parts of the brain, thus predominantly white matter, but underestimated for peripheral regions, such as cortical gray matter. In general, B_1 inhomogeneity leads to up to 8 pu (roughly 16 percent change) changes in MTR values at 3T.

The overall effect of B_1 correction is further analyzed using MTR histograms (Figure 5). As can be expected from Figure 4, B_1 correction leads to a shift of the whole-brain average MTR_{avg} histogram towards lower values (Figure 5A). In addition, the apparent shoulder in the MTR_{avg} histogram becomes markedly accentuated in the B_1-corrected MTR_c histogram, indicating the presence of (at least) two tissue classes (presumably WM and GM; cf. Figure 4B) with different MT properties that become more separated. Thus, the observed average and B_1-corrected whole brain MTR histograms are further analyzed based on the underlying, segmented, WM and GM (cf. Figures 5B and 5C). The fitting of the Gaussian model resulted in a MTR_{avg} peak at 48.05 pu with a cv = 0.100, and a MTR_c peak at 46.76 pu with a cv is 0.085 for bulk WM. Similarly, for bulk GM, the MTR_{avg} peak was at 39.76 pu with a cv = 0.213, whereas for MTR_c the maximum was at 38.48 pu and the cv was 0.230.

The results of the consecutive scan-rescanning are summarized in Figure 6. B_1-correction of MTR did not result in higher peak variability (standard deviation of the WM peak location changed from 0.15 pu to 0.12 pu and for GM from 0.15 pu and 0.09 pu after to B_1 correction), indicating a high stability for the B_1 measurement (Figure 6). While a repositioning of the volunteer and forcing a new scanner adjustment prior to any new MTR scan resulted in a higher variability for the MTR peak positions compared to the consecutive scan-rescan scenario, a lower variability was observed after B_1 correction (standard deviation of the WM peak location changed from 0.22 pu to 0.14 pu and for GM from 0.21 pu to 0.09 pu after B_1-correction) (Figure 7). This is in line with expectations since a different positioning will generally lead to slightly different B_1-field distributions. As a result, this is expected to become especially accentuated for brain MTR histograms extracted from different volunteers.

Finally, GM and WM MTR histograms are shown in Figure 8 for three volunteers of highly similar age (30y ± 2y). Average MTR_{avg} histograms for segmented WM and GM are depicted in Figures 8A and 8B. For WM, before B_1 correction the peaks varied within a range of 2.5 pu (46.8 pu to 49.3 pu), which was reduced to 0.9 pu (46.6 pu to 47.5 pu) after correction. Similarly, for GM, before B_1 correction the peaks varied within a range of 2.8 pu (38.7 pu to 41.5 pu), which was reduced to 2.0 pu (38.2 pu to 40.2 pu) after correction. Generally, B_1-correction of MTR values leads to a lower variability for MTR brain histograms, as can be expected for age-matched, normal appearing, brain tissue.

Discussion

A fast whole-brain MTR imaging method with intrinsic B_1-correction was introduced. The use of spiral imaging together with iterative parallel image reconstruction enabled an overall acquisition time for B_1-corrected MTR imaging of less than one minute for clinically acceptable resolutions. As a result, MTR scanning has the potential to be performed in the clinical routine setting without any significant workflow or patient throughput sacrifices.

Generally, non-uniform B_1-fields lead to a local variation of the applied MT-saturation power. As a result, even for a homogeneous tissue, any B_1-field variation will lead to a variation in the MT contrast, as long as an incomplete saturation can be presumed. Due to safety restrictions, however, saturation can never be complete, especially for in-vivo human MRI. As a result, all human MTR scans are subjected to B_1-field miscalibrations that become increasingly severe with increasing field strength.

A linear (first order) correction was suggested and implemented to remove the B_1-field related bias in derived MTR values; similar to previous studies and findings (24,26,27). For the suggested protocol, numerical simulations indicate that B_1-related MTR modulations become efficiently reduced. Generally, the quality of B_1-compensation relies on the longitudinal relaxation times and thus on the TR and flip angle settings and is expected to decrease with increasing T_1-weighting. In principle, it appears likely that this could be counterbalanced by a non-linear correction scheme, i.e. using a second order approach, but only at the expense of an overall prolonged scan time (using at least three MT-weighted scans).

In this work, we explored the limits for spiral whole brain MTR imaging in terms of resolution and acquisition speed. Since the proposed linear B_1-correction relies on the acquisition of PD to mildly T_1-weighted images, a rather long TR is required, as preferred by a 2D multi-slice protocol. As a result, scanning is typically performed with high in-plane but low slice resolution. Furthermore, efficient k-space sampling strategies, such as spiral readouts, can only accelerate imaging as long as the signal-to-noise-ratio (SNR) is not limiting. Similarly, resolution can only be increased at the expense of SNR. In summary, it can be expected that with decreasing SNR (and thus with increasing resolution), the proposed spiral imaging approach will offer decreasing benefits in terms of acquisition speed as compared to traditional Cartesian sampling schemes.

Using an integrated B_1-field map acquisition with (almost) no loss of scanning efficiency, we have shown in a scan-rescan experiment that B_1-corrected MTR values as compared to uncorrected ones are not subjected to a higher variability for consecutive scans but are less affected by repositioning and forced scanner readjustments. As a result, B_1-field correction might show added value for single patient follow-up studies, where typically special care is taken that scan-rescans can be performed on the same system (c.f. recommendations from the EURO-MT study, (39)). Our measurements, however, indicate that especially studies based on normative group comparisons, frequently used to assess diffuse

pathologic alterations in normal appearing brain tissue, such as for Alzheimer's disease (10,40,41), may profit from the removal of any B_1-field related variations. Generally, B_1-corrected MTR histograms should reveal a lower spread and thus group comparisons should require a smaller cohort size for a given effect size.

Conclusion

In conclusion, we have introduced a one-minute whole brain MTR mapping method, offering intrinsic B_1-field correction. Generally, B_1-field corrected MTR values show a lower variability in scan-rescan experiments as compared to uncorrected ones and might thus be especially beneficial within the context of follow-up studies or for the investigation of diffuse pathological changes based on large patient cohorts. Due to its speed, the proposed method thus not only shows excellent prospects for broad clinical translation but also for application in a variety of clinical studies that explore MT-effects based on a simple MTR analysis.

Acknowledgements

Swiss National Science Foundation, Grant/Award Number: SNF 325230_182008.

References

1. Wolff SD, Balaban RS. Magnetization transfer contrast (MTC) and tissue water proton relaxation in vivo. Magn. Reson. Med. 1989;10:135–144 doi: 10.1002/mrm.1910100113.

2. Paul Tofts. Quantitative MRI of the Brain: Measuring Changes Caused by Disease.; 2004.

3. Dousset V, Grossman RI, Ramer KN, et al. Experimental allergic encephalomyelitis and multiple sclerosis: lesion characterization with magnetization transfer imaging. Radiology 1992;182:483–491 doi: 10.1148/radiology.182.2.1732968.

4. Buchem MA van, Steens SCA, Vrooman HA, et al. Global Estimation of Myelination in the Developing Brain on the Basis of Magnetization Transfer Imaging: A Preliminary Study. Am. J. Neuroradiol. 2001;22:762–766.

5. Spilt A, Geeraedts T, Craen AJM de, Westendorp RGJ, Blauw GJ, Buchem MA van. Age-Related Changes in Normal-Appearing Brain Tissue and White Matter Hyperintensities: More of the Same or Something Else? Am. J. Neuroradiol. 2005;26:725–729.

6. Waesberghe JHTMV, Kamphorst W, Groot CJAD, et al. Axonal loss in multiple sclerosis lesions: Magnetic resonance imaging insights into substrates of disability. Ann. Neurol. 1999;46:747–754 doi: 10.1002/1531-8249(199911)46:5<747::AID-ANA10>3.0.CO;2-4.

7. Barbosa S, Blumhardt LD, Roberts N, Lock T, Edwards RHT. Magnetic resonance relaxation time mapping in multiple sclerosis: Normal appearing white matter and the “invisible” lesion load. Magn. Reson. Imaging 1994;12:33–42 doi: 10.1016/0730-725X(94)92350-7.

8. Filippi M, Campi A, Dousset V, et al. A Magnetization Transfer Imaging Study of Normal-Appearing White Matter in Multiple Sclerosis. Neurology 1995;45:478 doi: 10.1212/WNL.45.3.478.

9. Loevner LA, Grossman RI, Cohen JA, Lexa FJ, Kessler D, Kolson DL. Microscopic disease in normal-appearing white matter on conventional MR images in patients with multiple sclerosis: assessment with magnetization-transfer measurements. Radiology 1995;196:511–515 doi: 10.1148/radiology.196.2.7617869.

10. Flier WMVD, Heuvel DMJVD, Weverling-Rijnsburger AWE, et al. Magnetization transfer imaging in normal aging, mild cognitive impairment, and Alzheimer’s disease. Ann. Neurol. 2002;52:62–67 doi: 10.1002/ana.10244.

11. Grossman RI. Magnetization transfer in multiple sclerosis. Ann. Neurol. 1994;36:S97–S99 doi: 10.1002/ana.410360722.

12. Gass A, Barker GJ, Kidd D, et al. Correlation of magnetization transfer ration with clinical disability in multiple sclerosis. Ann. Neurol. 1994;36:62–67 doi: 10.1002/ana.410360113.

13. Buchem MA van, Udupa JK, McGowan JC, et al. Global volumetric estimation of disease burden in multiple sclerosis based on magnetization transfer imaging. Am. J. Neuroradiol. 1997;18:1287–1290.

14. Ropele S, Fazekas F. Magnetization transfer MR imaging in multiple sclerosis. Neuroimaging Clin. N. Am. 2009;19:27–36 doi: 10.1016/j.nic.2008.09.004.

15. Horsfield MA. Magnetization Transfer Imaging in Multiple Sclerosis. J. Neuroimaging 2005;15:58S-67S doi: 10.1177/1051228405282242.

16. Kalkers NF, Hintzen RQ, van Waesberghe JHTM, et al. Magnetization transfer histogram parameters reflect all dimensions of MS pathology, including atrophy. J. Neurol. Sci. 2001;184:155–162 doi: 10.1016/S0022-510X(01)00431-2.

17. Filippi M, Iannucci G, Tortorella C, et al. Comparison of MS clinical phenotypes using conventional and magnetization transfer MRI. Neurology 1999;52:588 doi: 10.1212/WNL.52.3.588.

18. Davies GR, Ramió-Torrentà L, Hadjiprocopis A, et al. Evidence for grey matter MTR abnormality in minimally disabled patients with early relapsing-remitting multiple sclerosis. J. Neurol. Neurosurg. Amp Psychiatry 2004;75:998 doi: 10.1136/jnnp.2003.021915.

19. Buchem MA van, McGowan JC, Kolson DL, Polansky M, Grossman RI. Quantitative volumetric magnetization transfer analysis in multiple sclerosis: Estimation of macroscopic and microscopic disease burden. Magn. Reson. Med. 1996;36:632–636 doi: 10.1002/mrm.1910360420.

20. Ge Y, Grossman RI, Babb JS, Rabin ML, Mannon LJ, Kolson DL. Age-related total gray matter and white matter changes in normal adult brain. Part II: quantitative magnetization transfer ratio histogram analysis. AJNR Am. J. Neuroradiol. 2002;23:1334–1341.

21. Tofts PS, Steens SCA, Cercignani M, et al. Sources of variation in multi-centre brain MTR histogram studies: body-coil transmission eliminates inter-centre differences. Magn. Reson. Mater. Phys. Biol. Med. 2006;19:209–222 doi: 10.1007/s10334-006-0049-8.

22. Graham SJ, Henkelman RM. Understanding pulsed magnetization transfer. J. Magn. Reson. Imaging 1997;7:903–912 doi: 10.1002/jmri.1880070520.

23. Pike GB, Glover GH, Hu BS, Enzmann DR. Pulsed magnetization transfer spin-echo MR imaging. J. Magn. Reson. Imaging 1993;3:531–539 doi: 10.1002/jmri.1880030316.

24. Ropele S, Filippi M, Valsasina P, et al. Assessment and correction of B1-induced errors in magnetization transfer ratio measurements. Magn. Reson. Med. 2005;53:134–140 doi: 10.1002/mrm.20310.

25. Helms G, Dathe H, Dechent P. Modeling the influence of TR and excitation flip angle on the magnetization transfer ratio (MTR) in human brain obtained from 3D spoiled gradient echo MRI. Magn. Reson. Med. 2010;64:177–185 doi: 10.1002/mrm.22379.

26. Volz S, Nöth U, Rotarska-Jagiela A, Deichmann R. A fast B1-mapping method for the correction and normalization of magnetization transfer ratio maps at 3 T. NeuroImage 2010;49:3015–3026 doi: 10.1016/j.neuroimage.2009.11.054.

27. Samson RS, Wheeler-Kingshott CAM, Symms MR, Tozer DJ, Tofts PS. A simple correction for B1 field errors in magnetization transfer ratio measurements. Magn. Reson. Imaging 2006;24:255–263 doi: 10.1016/j.mri.2005.10.025.

28. Yarnykh VL, Khodanovich MYu. Analytical Method of Correction of B1 Errors in Mapping of Magnetization Transfer Ratio in Highfield Magnetic Resonance Tomography. Russ. Phys. J. 2015;57:1784–1788 doi: 10.1007/s11182-015-0451-7.

29. Ma D, Gulani V, Seiberlich N, et al. Magnetic resonance fingerprinting. Nature 2013;495:187–192 doi: 10.1038/nature11971.

30. Heule R, Pfeuffer J, Meyer CH, Bieri O. Simultaneous B1 and T1 mapping using spiral multislice variable flip angle acquisitions for whole-brain coverage in less than one minute. Magn. Reson. Med. 2019;81:1876–1889 doi: 10.1002/mrm.27544.

31. Meyer CH, Zhao L, Lustig M, et al. Dual-Density and Parallel Spiral ASL for Motion Artifact Reduction. Proc Intl Soc Magn Reson Med 19:3986.

32. Heule R, Pfeuffer J, Bieri O. Snapshot whole-brain T1 relaxometry using steady-state prepared spiral multislice variable flip angle imaging. Magn. Reson. Med. 2018;79:856–866 doi: 10.1002/mrm.26746.

33. Tan H, Meyer CH. Estimation of k-space trajectories in spiral MRI. Magn. Reson. Med. 2009;61:1396–1404 doi: 10.1002/mrm.21813.

34. Mugler III JP, Brookeman JR. Rapid three-dimensional T1-weighted MR imaging with the MP-RAGE sequence. J. Magn. Reson. Imaging 1991;1:561–567.

35. Lustig M, Pauly JM. SPIRiT: Iterative self-consistent parallel imaging reconstruction from arbitrary k-space. Magn. Reson. Med. 2010;64:457–471 doi: 10.1002/mrm.22428.

36. Stollberger R, Wach P. Imaging of the active B1 field in vivo. Magn. Reson. Med. 1996;35:246–251 doi: 10.1002/mrm.1910350217.

37. Ganter C. Configuration Model. In: Proc. Intl. Soc. Mag. Reson. Med. 26. France; 2018. p. 5663.

38. Pike GB. Pulsed magnetization transfer contrast in gradient echo imaging: A two-pool analytic description of signal response. Magn. Reson. Med. 1996;36:95–103 doi: 10.1002/mrm.1910360117.

39. Barker GJ, Schreiber WG, Gass A, et al. A standardised method for measuring magnetisation transfer ratio on MR imagers from different manufacturers—the EuroMT sequence. Magn. Reson. Mater. Phys. Biol. Med. 2005;18:76–80 doi: 10.1007/s10334-004-0095-z.

40. Bozzali M, Franceschi M, Falini A, et al. Quantification of tissue damage in AD using diffusion tensor and magnetization transfer MRI. Neurology 2001;57:1135 doi: 10.1212/WNL.57.6.1135.

41. Kabani NJ, Sled JG, Chertkow H. Magnetization Transfer Ratio in Mild Cognitive Impairment and Dementia of Alzheimer's Type. NeuroImage 2002;15:604–610 doi: 10.1006/nimg.2001.0992.

Figure Captions

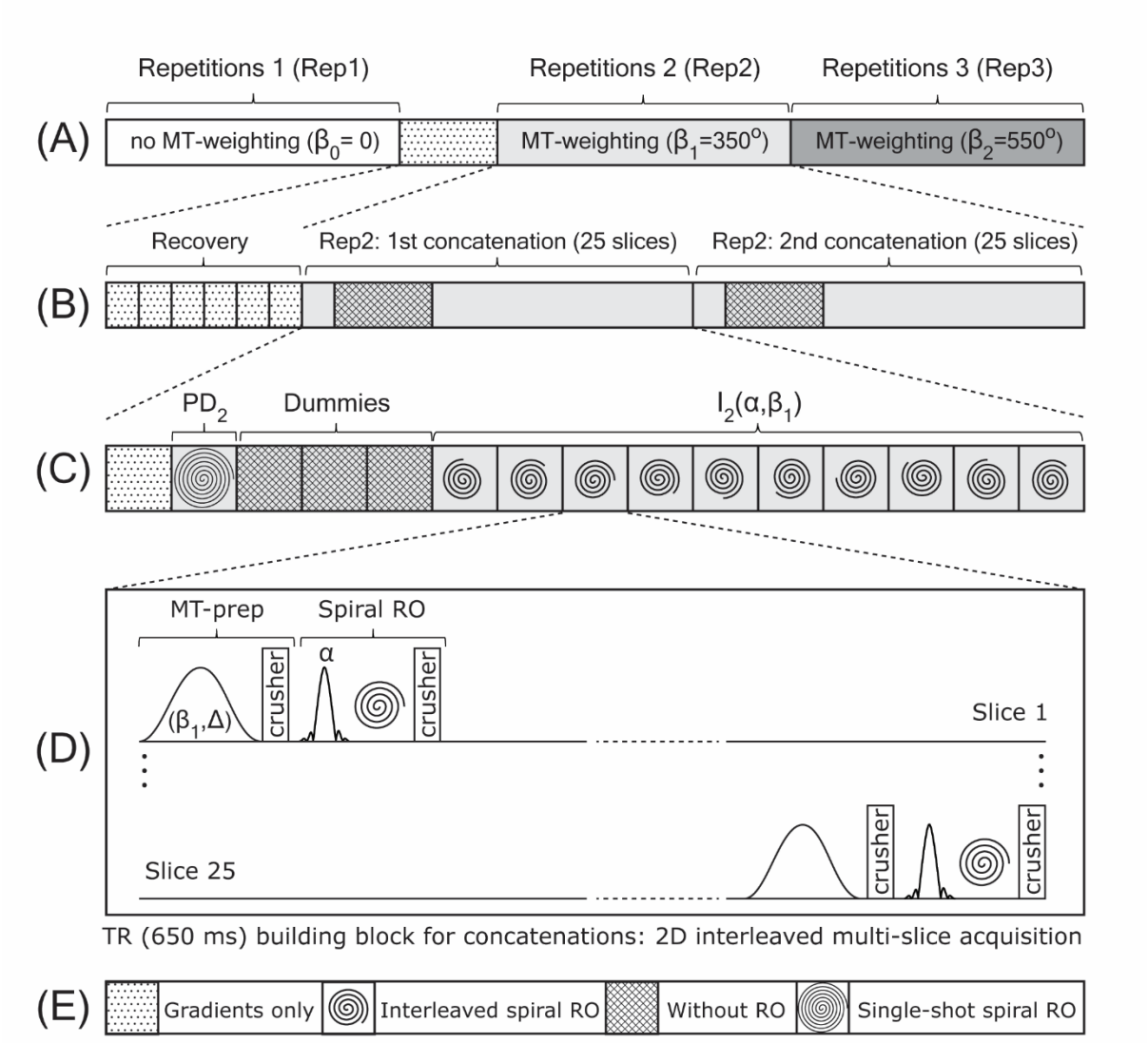

Figure 1: Scheme of the prototype 2D interleaved multi-slice spiral MTR imaging approach. (A) three repetitions are acquired with different MT-weightings (β: MT-saturation flip angle). (B) Each repetition features two concatenations with 25 slices each (50 slices in total). Between repetition one and two an additional delay of six TR (about 4 s) allows for full recovery of the concatenations. (C) Each concatenation starts with a single-shot spiral TR, yielding low-resolution PD-weighted images, followed by a dummy period of three TR (about 2 s) without readout (RO), and being terminated by the acquisition of high-resolution PD to mildly T_1-weighted images using a series of N spiral interleaves (N=20). (D) Building block illustrated for one spiral interleave within the 1st concatenation of repetition 2 of the 2D interleaved multi-slice acquisition. The TR is built from 25 interleaved MT-prepared (Δ: off-resonance) slice excitations (flip angle α). (E) legend.

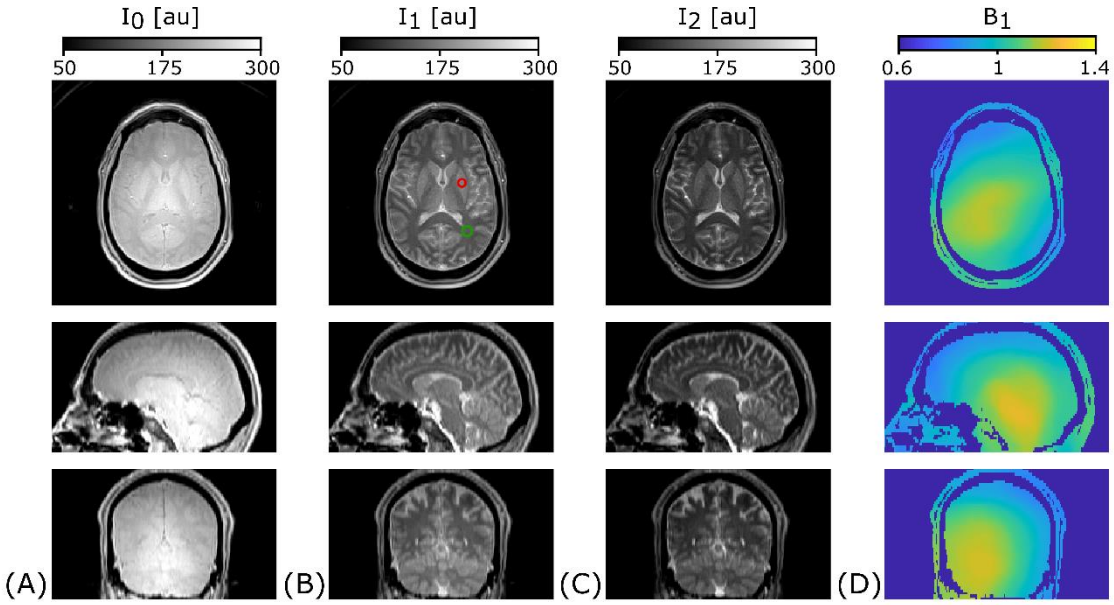

Figure 2: Illustrative axial, sagittal and coronal views of: non-MT-weighted images (A), MT-weighted images acquired with an MT-saturation flip angle of 350° (B), MT-weighted images acquired with an MT-saturation flip angle of 550° (C), and a corresponding B1-map (D), derived from PD_1 and PD_2 (c.f. Figure 1).

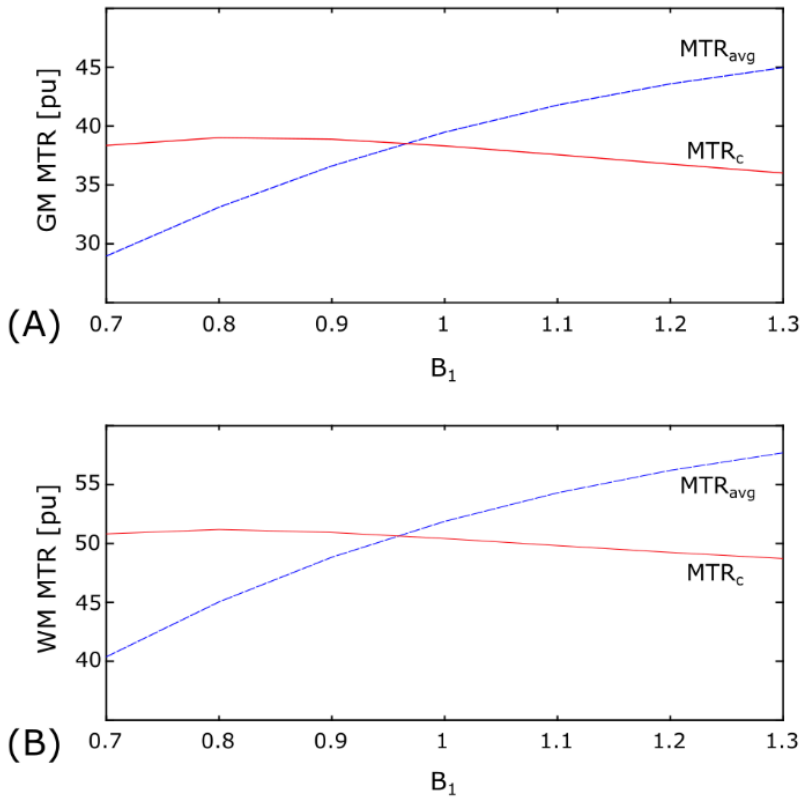

Figure 3: Two-pool model simulations of the B_1-dependency of MTR for (A) GM and (B) WM before (MTR_{avg}: dashed blue line) and after correction (MTR_c: solid red line) using Eq [3] (for simulation parameters, see 'Methods' section).

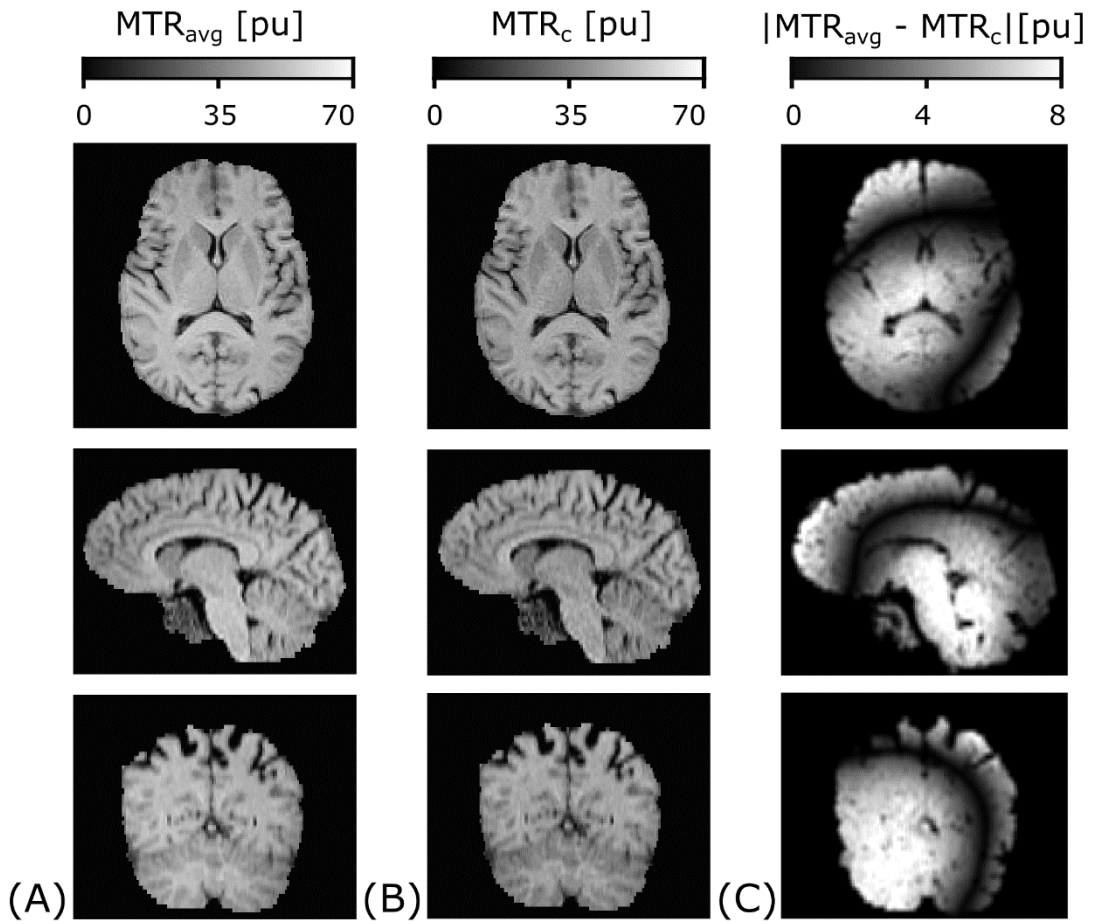

Figure 4: Example views in axial, sagittal and coronal orientation of average MTR_{avg} (A) and B_1-corrected MTR_c (B) together with the corresponding absolute difference map (C).

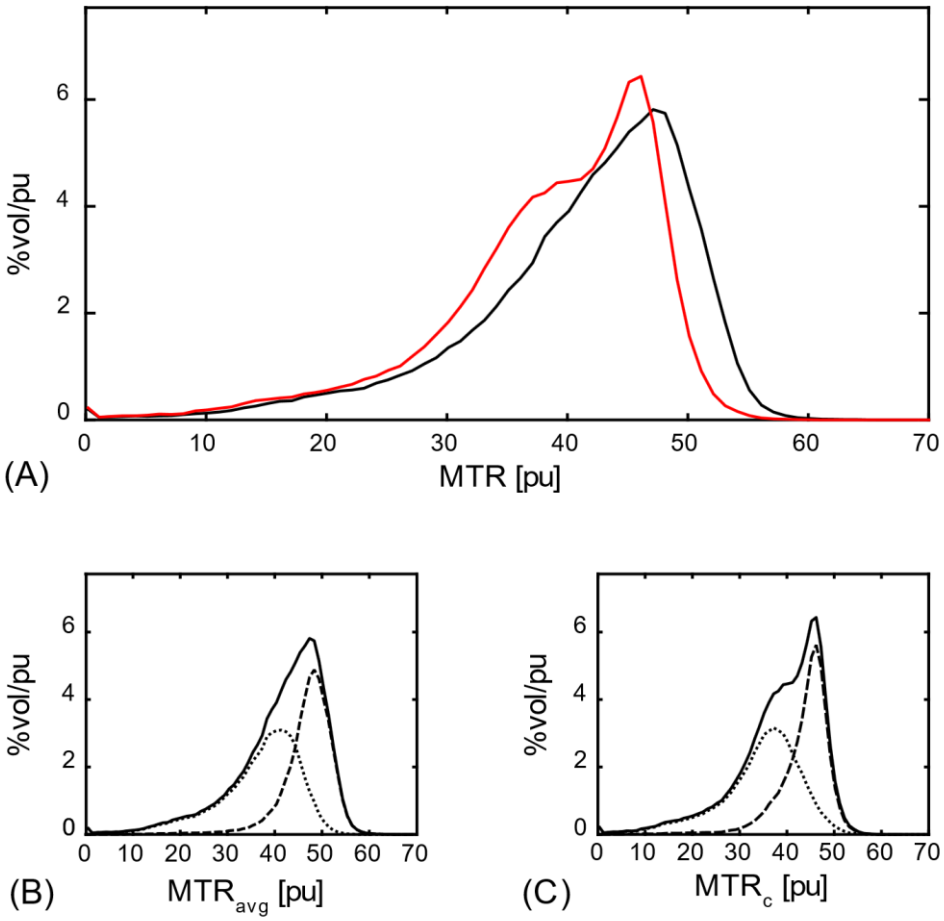

Figure 5: (A) Whole brain histograms for average (black solid line) and B_1-corrected (red solid line) MTR values of an exemplary subject (B) Average MTR_{avg} histogram (black solid line) segmented into WM (black dashed line) and GM (black dotted line). (C) B_1-corrected MTR_c histogram (black solid line) segmented into WM (black dashed line) and GM (black dotted line).

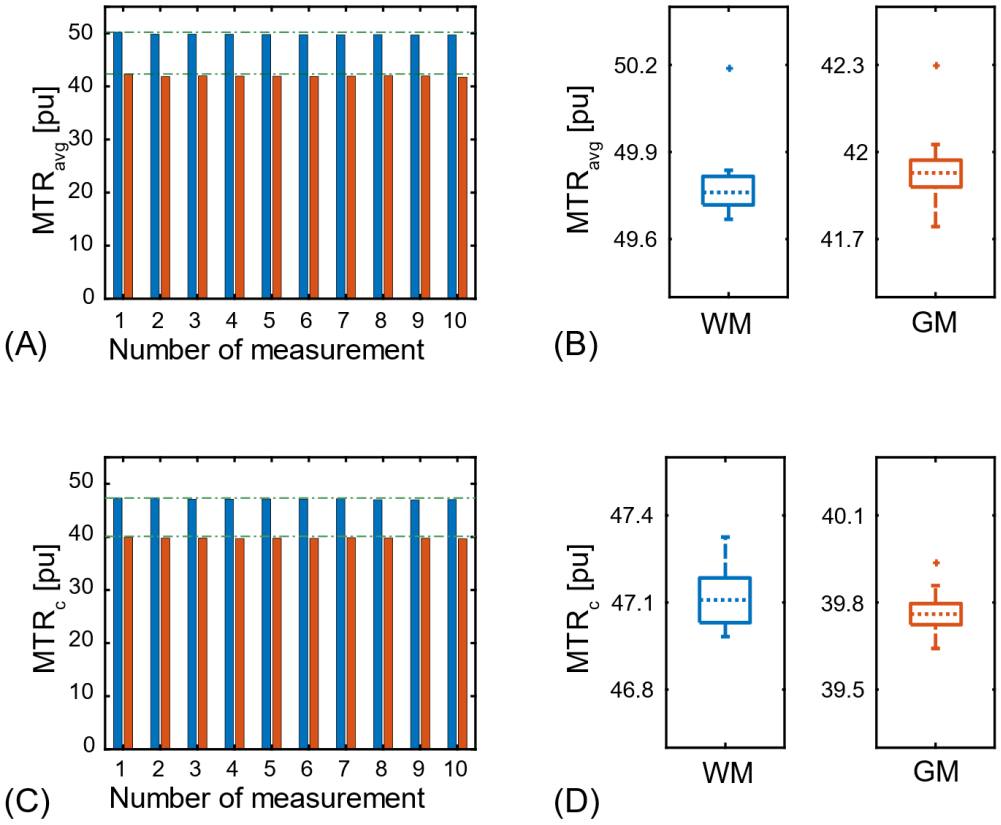

Figure 6: Repeatability assessment from scan-rescan experiments (without repositioning) using an MTR histogram peak analysis as shown in Figure 5. (A) Average MTR_{avg} peak values for segmented GM (orange) and WM (blue). (B) Corresponding boxplots, showing median, lower and upper quartiles, as well as the maximum and minimum values. (C) B_1-corrected MTR_c peak values for segmented GM (orange) and WM (blue). (D) Corresponding boxplots, showing median, lower and upper quartiles, as well as the maximum and minimum values.

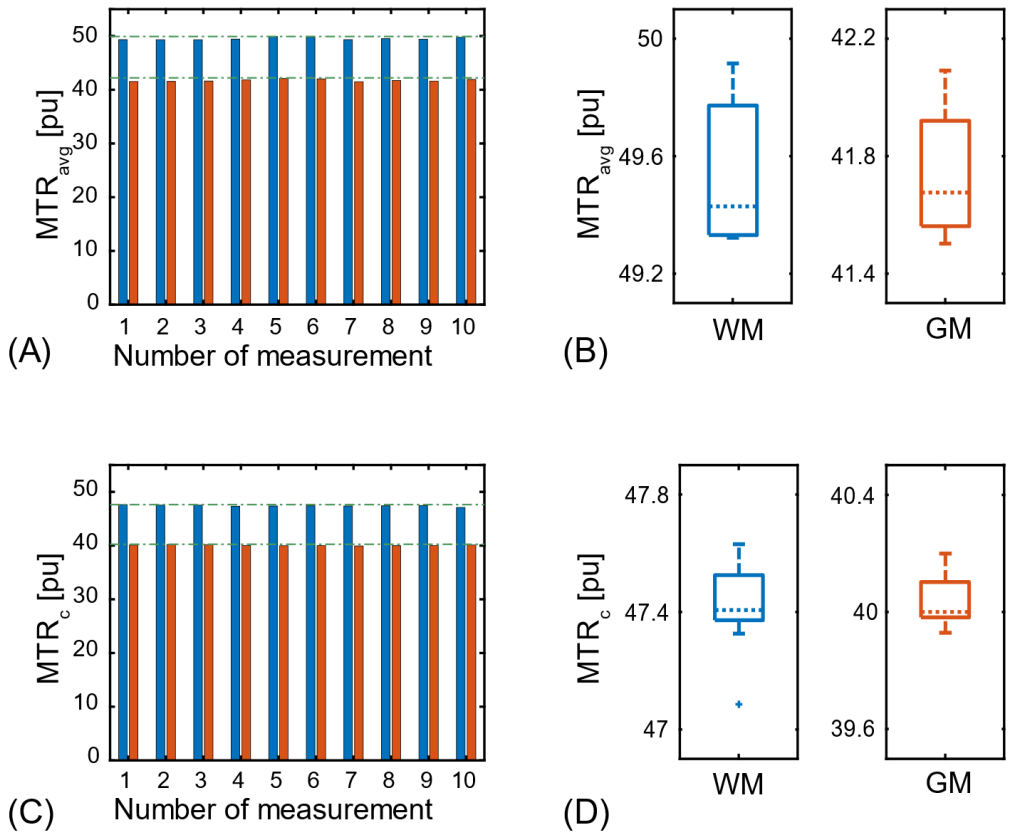

Figure 7: Reproducibility assessment from scan-rescan experiments (with repositioning) using an MTR histogram peak analysis as shown in Figure 5. (A) Average MTR_{avg} peak values for segmented GM (orange) and WM (blue). (B) Corresponding boxplots, showing median, lower and upper quartiles, as well as the maximum and minimum values. (C) B_1-corrected MTR_c peak values for segmented GM (orange) and WM (blue). (D) Corresponding boxplots, showing median, lower and upper quartiles, as well as the maximum and minimum values.

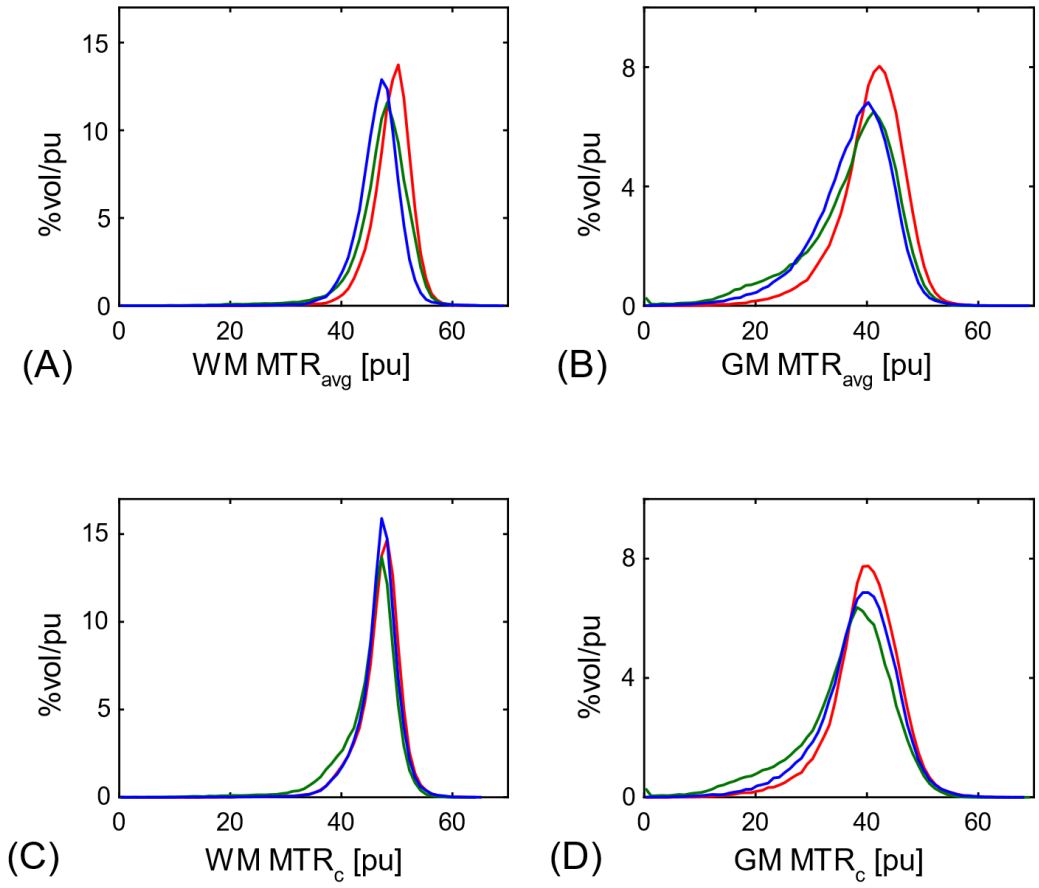

Figure 8: Average MTR_{avg} histograms for three age-matched healthy volunteers for segmented WM (A) and GM (B). Corresponding B_1-corrected MTR_c histograms for segmented WM (C) and GM (D).